Improved Threat Detection in Walk-Through Security Scanning Using an Optimized Polarimetric Target Decomposition Method

KONSTANTIN ROOT [1], JULIAN ADAMETZ[1], FRANK GUMBMANN [2], INGRID ULLMANN [1], AND MARTIN VOSSIEK [1] (Fellow, IEEE)

(Regular Paper)

[1]Institute of Microwaves and Photonics, Friedrich-Alexander-Universität Erlangen-Nürnberg, 91058 Erlangen, Germany
[2]Rohde & Schwarz GmbH & Co. KG, 81671 Munich, Germany

CORRESPONDING AUTHOR: Konstantin Root (e-mail: konstantin.root@fau.de).

ABSTRACT Reliable and convenient walk-through security scanning, which doesn't separate people or impede their movement, is an extremely challenging task. In this paper, a novel approach for a security check with an overhead observation and a polarimetric target decomposition is presented. The viewing angle of the scanner equals a side-looking airborne radar. However, it will be shown that the established polarimetric target decomposition methods of remote-sensing are not well suited for close-range radar imaging and need to be adapted due to the differences in the geometry of the imaging scenario. The usage of a multiple input and multiple output (MIMO) array and the shorter distance between array and target need a changed decomposition technique in order to distinguish between persons with or without worn threat objects. The differences between radar remote-sensing and close-range imaging scenarios are investigated. An optimized version of the Sato four-component polarimetric scattering decomposition is derived. The proposed close-range adjustment is applied to the model and investigated experimentally with a 4-to-12 GHz fully polarimetric MIMO imaging system. Polarimetric decomposition is carried out on defined test structures with known scattering mechanisms, as well as on mannequins and persons with different threat objects like guns or explosives. In test campaigns, promising results were achieved for a correct target decomposition in radar-based walk-through security scanning.

INDEX TERMS MIMO radar, polarimetry, decomposition, radar imaging, security scanning.

I. INTRODUCTION

Nowadays, most terror attacks happen in easily accessible, public, and crowded places, with the result that they cause the greatest possible damage. Even though terrorists are equipped with heavy guns and explosive vests, assaults cannot be prevented because of a lack of missing security checks. Although a wide variety of security radar scanners are available, they are all poorly suited for use in public places. Nowadays, most systems require people to stand still [1] during the scanning time to create a radar image. Whereas newer walk-through systems can scan people as they pass by [2]. The former type of scanner takes a long time to scan people and so it is not suitable for

large crowds. Walk-through scanners have a higher throughput and hence can scan a greater number of people in a given time, which is a property that is very useful for an application in crowded places. However, currently, all presented walk-through scanners are located at the height of persons. This allows a good illumination of people passing through the scanner and yields the best achievable image quality. Nevertheless, this property comes with a disadvantage: if a group of people passes through the scanner at the same time, it is possible that some people are covered and, consequently, not properly scanned. Because of such covering, there is a possibility of unauthorized objects being brought in unnoticed. This threat
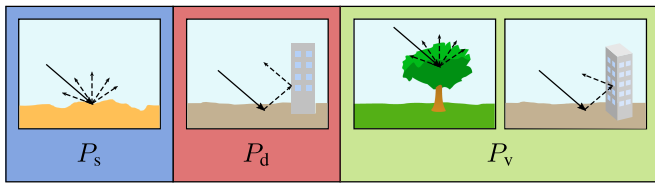
FIGURE 1. Single, double, and volume scattering power for the applied decomposition algorithm [9].

can be avoided, however, if the group is split and every person is scanned separately. Certainly, the separation limits the maximal throughput and in very crowded places like train stations or football stadiums, this kind of application becomes impossible. Furthermore, due to the mandatory separation of people, there is a need to restrict hallways with barriers and thus force people to walk through the scanners. However, the barriers and the narrowness way-through of the scanners restrict also staff and their workflows. Health care, escape paths, maintenance, catering, etc., are impeded. Consequently, walk-through systems have some considerable disadvantages.

In this paper, a novel approach for a security check with an overhead observation and a polarimetric target decomposition is presented. The viewing angle of the scanner equals a side-looking airborne radar. The modified positioning of the radar modules does not impact the stream of people and allows an unchanged throughput. However, due to the changed observation location, the illumination property deteriorates, leading to a coarse imaging result, in which reflections are hard to interpret. To compensate for the disadvantage of the new positioning, a polarimetric target decomposition technique is used.

There are three different main approaches for target decomposition: Mueller-Matrix based decomposition, Eigenvector analysis, and coherent decomposition of matrices of scattering models [3]. All three techniques show good performance in remote-sensing scenarios, but compared to Eigenvector- and Mueller-Matrix based decomposition, the model-based decomposition has a high computational efficiency, is physically easy to understand, and is easily adjustable [4]. A time efficient decomposition technique is mandatory in our case since a security application in crowded places with a high volume of people is investigated. Decompositions based on Eigenvector- or Mueller-Matrix seem therefore less suited than computational efficient model-based decompositions and hence, won't be further investigated. Model-based decomposition techniques assume physical scattering models with structures like soils, buildings, or vegetation. The co- and cross-polarized signals received from these structures are unique and can therefore distinguish between single, double, and volume scattering. Examples for the scattering processes and their contribution to the corresponding scattering power are given in Fig. 1. Started in 1993 by Freeman and Durden with a simple three-component scattering model [5], many scientists have researched this topic. Since the measured polarimetric information is not fully evaluated in this three-component model, new calculation procedures, or scattering

models were added to the decomposition [4]. Helix scattering [6], different models for dipole scattering [7], [8] and dihedral structures [9], [10] have been introduced and yielded a seven-component target decomposition model [11].

Possible reflections in security screening scenarios are similar to remote-sensing reflections. Most terrorists wear a gun and a heavy explosive vest to cause as much damage as possible. Additionally, explosives are combined with shrapnels like nails or screws for an even higher impact. The human torso acts as a big smooth surface without any edges and thus, predominantly single-bounces can be expected from a human body without any hidden objects. Carried guns or explosives placed at the body form a double-bounce structure with the skin, so creating a different reflection signature than blank skin. A piece of shrapnel such as a screw can be thought of as dipoles. Many arbitrarily orientated screws act like a dipole cloud, demonstrating a volume scattering process. Since only these three main scattering processes are of interest, the proposed four-component decomposition from Sato et al. [9] will be used. Although the fourth component (helix scattering) is not relevant, this model has an improved detection of oriented double-bounce structures compared to previous models [12] and seems to be suited for an application in security screening. With a large MIMO array and hence many different observation angles, these geometries can be expected, too.

Although scattering processes are quite similar in remote-sensing and security controls, decomposition cannot be used right away in close-range. This paper investigates and explains in Section II the differences in remote imaging with an airborne and a MIMO radar in close-range. The necessary adjustment of the known decomposition technique to this novel close-range application will be presented in Section III. The new acquired decomposition model is verified in Section IV with defined test structures, before being further tested with realistic security scenarios. Finally, Section V gives a summary of this work.

II. DIFFERENCES OF SCATTERING PROCESSES IN REMOTE-SENSING AND CLOSE-RANGE SCENARIOS
A. POLARIMETRIC TARGET DECOMPOSITION

The decomposition method studied here is a four-component, model-based method by Sato et al. [9]. In this method, canonical scattering processes are used as a base for modeling the scattering matrix. These scattering processes can be described by their scattering or Sinclair matrix $[S]$, with

$$S = \begin{bmatrix} S_{HH} & S_{HV} \\ S_{VH} & S_{VV} \end{bmatrix}. \tag{1}$$

The copolarized reflectivity is represented by S_{HH} and S_{VV} for the horizontal and vertical electric field. Whereas S_{VH} and S_{HV} designate the occurring cross-polarized reflected power. Based on the radar images obtained for every copolarized and cross-polarized channel, the coherency matrix needs to be calculated from the Pauli vector, which is for monostatic

systems defined as

$$k_\mathrm{p} = \frac{1}{\sqrt{2}} \begin{bmatrix} S_\mathrm{HH} + S_\mathrm{VV} \\ S_\mathrm{HH} - S_\mathrm{VV} \\ 2S_\mathrm{HV} \end{bmatrix}, \tag{2}$$

and leads to the ensemble average coherency matrix with

$$\langle[T]\rangle = \langle k_\mathrm{p} k_\mathrm{p}^\dagger \rangle, \tag{3}$$

where $\dagger$ is the conjugate transpose operator and $\langle\rangle$ denotes the ensemble average. The S_VH and S_HV components for monostatic systems can be assumed as equal, but differ for bistatic systems [18]. However, for our later investigated MIMO system we assume $S_\mathrm{VH} = S_\mathrm{HV}$, too. The measured magnitudes and phase information for the cross-polarized images with 16 Tx and 32 Rx antennas result in 512 bistatic antenna configurations. Based on the fact, that each 512 antenna combinations are processed to one radar image, an effective phase center for each polarization channel can be described [13]. With a similar array geometry for the horizontal and vertical polarized antennas, the effective phase centers for all polarization channels are located at a similar place. Furthermore, we expect that differences in the scattering magnitude from targets for the bistatic configuration are in total averaged for all antenna combinations, too. The two aforementioned considerations lead us to the assumption, that magnitude and phase information of S_VH and S_HV can be approximated as similar.

After minimization of the T_{33} element by the determined rotation angle [12][14], the rotated coherency matrix $\langle[T']\rangle$ can be expanded into

$$\langle[T']\rangle = f_\mathrm{s}\langle[T]\rangle_\mathrm{surface} + f_\mathrm{d}\langle[T]\rangle_\mathrm{double}$$
$$+ f_\mathrm{v}\langle[T]\rangle_\mathrm{vol} + f_\mathrm{c}\langle[T]\rangle_\mathrm{helix}, \tag{4}$$

with the corresponding submatrices for surface, double-bounce, volume, and helix scattering, and the to-be-determined coefficients f_s, f_d, f_v, and f_c. The last-called scattering mechanism produces circular polarization. Due to its low contribution to the total power [6], [12], this scattering process is here not considered further.

Equation (4) indicates that the total power P_t of the scattering matrix $[S]$ is distributed to all scattering processes for every pixel in the radar image as

$$P_\mathrm{t} \propto P_\mathrm{s} + P_\mathrm{d} + P_\mathrm{v} + P_\mathrm{c} = \langle|S_\mathrm{HH}|^2 + |S_\mathrm{VV}|^2 + 2|S_\mathrm{HV}|^2\rangle. \tag{5}$$

As it can be seen in Equation (5), a difference for the reflectivity properties of each individual scattering process in the imaging scenario leads also to a difference of the power detected for each scattering process. This power mismatch may lead to a distorted decomposition result, since the total power P_t is proportional to the sum of each scattering power. This imbalance, along with the large values of the diagonal elements of the coherency matrix compared to the other elements, were described in [15] and [16], respectively. Both authors suggested weighting factors for a compensation. The source for the imbalance is not further investigated in [16] and

the values for the weighting factors were calculated by the mean values of the coherency matrix entries from six different remote-sensing data sets. Each matrix element was then multiplied with the averaged inverse factor, putting all entries at a similar magnitude. Even though this procedure improved the decomposition result, the calculation is not generally valid, since an equal distribution of all scattering processes has to be assumed. If a data set lacks one scattering process, the corresponding coherency matrix entries will be quite low and the compensation factor will increase the values to an incorrect level. A more general investigation for close-range scenarios was done in [15]. The weighting factors were introduced in the decomposition equation and a calculation procedure was suggested. Since the calculation method is abstract, based on simplified assumptions, and on observations made by measurements, a more general solution is given here. Similar to the idea of model-based polarimetric decomposition, where Sinclair matrices from physical models describe their scattering behavior, the resulting differences of the coherency matrix entries are investigated by physical scattering models.

At first, due to the changed measurement scenario and scattering mechanisms, the differences in close-range and remote-sensing are investigated. In remote-sensing, polarimetric measurements are done by a side-looking radar, where an airplane or satellite carries a mobile radar system and scans the imaging scene under a certain elevation angle, at a great distance. Due to the monostatic setup, rough scattering surfaces, and the oblique angle of incidence, only signals from diffuse scattering targets are received. On the other hand, close-range security scanners work with a very low power level and hence, aim to illuminate a person as thoroughly as possible. For this purpose, a MIMO array in these scanners is used and detects mostly strong, specular reflections from the human skin. The distance between the array and the person being scanned is usually small. The effects of this specular reflection and closer distance in the security application will be explained in detail.

B. SPECULAR REFLECTION VS. DIFFUSE REFLECTION

The aforementioned effects of specular and diffuse reflections can be seen in Figs. 2 and 3. The images show simulation results for an emitted and scattered electric field, E_e and E_s for two different scattering objects. The chosen geometry, coordinates, and frequency of the simulation correspond to the imaging scenario and array properties of the measurements in section IV. Based on the vector wave equation [17], the scattered electric field orientated in x-direction, can be described by

$$E_\mathrm{s}(\vec{r}) = -\int_S \frac{\partial}{\partial z} E_\mathrm{e}(\vec{r}')g(\vec{r}, \vec{r}')d\vec{r}',' \tag{6}$$

S is the surface of the scattering object and $g(\vec{r}, \vec{r}')$ is the Green's function. In the simulation, an electric field with a frequency of $f = 7.75\,\mathrm{GHz}$ is emitted from the position $x = -0.75\,\mathrm{m}$, $z = 0$. At the coordinates $x = 0$, $z = 1.6\,\mathrm{m}$ a flat metal plate, and a rough dipole cloud, respectively, were
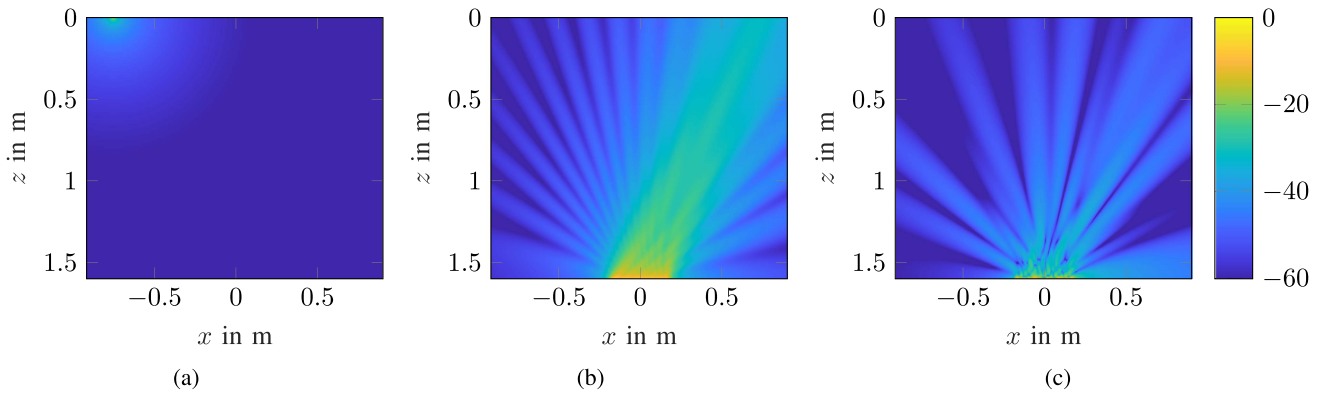
FIGURE 2. Electric field intensity for (a) an emitted wave and scattered wave by (b) a flat metal plate, and (c) rough dipole cloud, respectively. The dimensions of both scattering targets are equal, but their reflectivity properties differ due to their surface roughness. The value of the electric field is normalized to each maximum field intensity and calculated in dB.
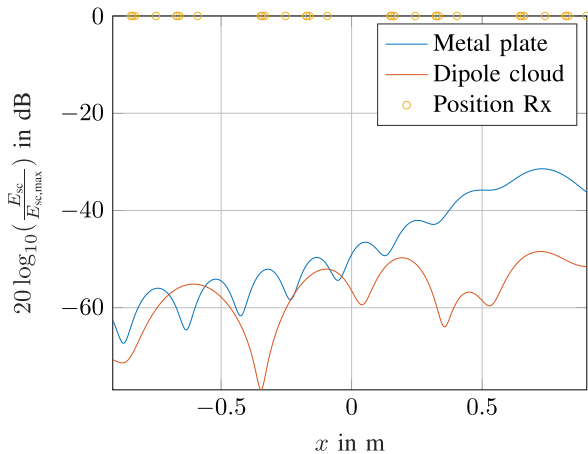

FIGURE 3. Comparison of the electric field intensity at the position of the MIMO array. The signal received from the metal plate has a higher intensity level than the one received from the dipole cloud.

assumed with point scatterers. The metal plate was simulated as a perfect electric conductor. The point scatterers of the dipole cloud have a normal distributed reflectivity between 0 and 1, simulating different orientations of dipoles in respect to the orientation of the electric field vector [18]. Both scattering objects have a width of approximately 35 cm, and the roughness of the dipole cloud is a quarter wavelength, namely $\lambda/4 = 9.7$ mm.

Fig. 2 shows the electric field intensity of the incident and scattered wave. It can be seen, that the metal plate produces a specular reflection, where the emergent angle of the main lobe equals the incident angle. Whereas the dipole cloud has a diffuse reflectivity property with no distinct main lobe. In Fig. 3, it can be seen, that this fact has no negative effect for polarimetric decomposition in remote-sensing scenarios. As mentioned before, the monostatic setup means that Tx- and Rx-antenna are at the same position ($x = -0.75$ m, $z = 0$) and as shown in Fig. 3, the field intensities at this position are very similar for both types of reflections. Hence, the

decomposition algorithm would detect single-bounce and volumetric scattering similarly well. Whereas in close-range with a MIMO array many field intensities at different positions are measured. Fig. 3 also shows the positions of the Rx-antennas of the imaging array. The specular reflection causes strong field intensities around $x = 0.75$ m and is much greater than the reflected field from the dipole cloud. Using the measured signals for every Rx-antenna, the image intensity in the reconstructed image is much greater for the metal plate and thus, a decomposition algorithm tends to detect single-bounces rather than volumetric scattering.

C. CLOSE-RANGE VS. LONG RANGE

As already explained in Section II II-B, imaging in close-range is dominated by strong specular reflections, and the same holds for double-bounce structures. In this case, geometrical optics can be applied for a determination of signal paths between Tx- and Rx-antennas (see Fig. 4). In the simulation, a plane surface and a double-bounce structure were placed at a 1.6 m distance from the array. The simulation yields a path length difference between single and double-bounce rays of $\Delta l_1 = 1.4$ cm and $\Delta l_2 = 1.6$ mm, for a antenna spacing of $d_1 = 30$ cm and $d_2 = 10$ cm. The bigger the spacing d between antenna pairs, the bigger the length difference Δl becomes. Additionally, it can also be seen, that for a greater distance between antennas and scattering structure, Δl decreases, and vice versa. This means for a very large distance like in remote-sensing, the different path length can be neglected. However, this affects radar imaging in close-range scenarios if double-bounces occur. For a MIMO array with many spatially distributed Tx- and Rx-antennas, this results in different possible scatterer distances for one target. After measuring, imaging can for example be done by holographic image reconstruction [19]. Therefore, the received signal s_r is correlated with a hypothesis s_{hyp}, which assumes a reflection from a point scatterer at a certain voxel position $p(x, y, z)$. This is done for every possible Tx-Rx-antenna combination and the correlation for an investigated voxel is summed up for
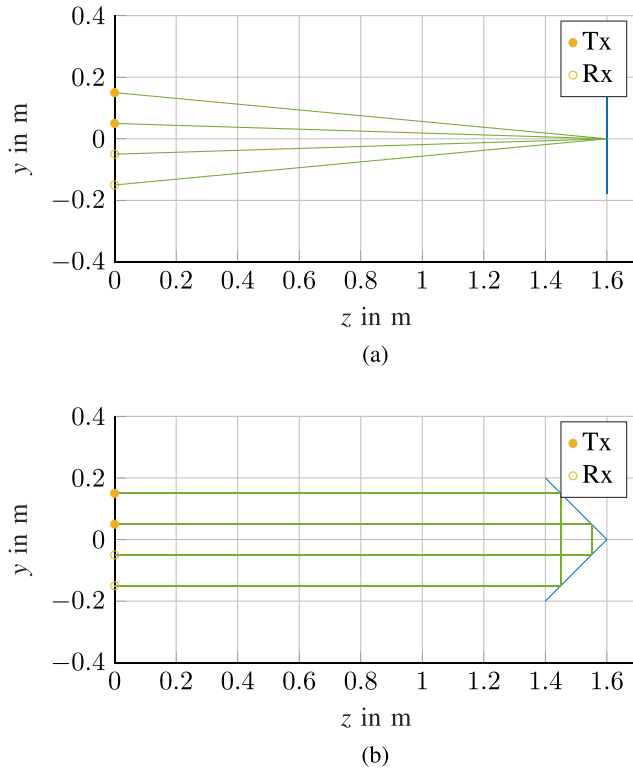
(a)

(b)

FIGURE 4. Different ray paths between Tx- and Rx-antennas for a specular reflection from (a) a flat surface and (b) double-bounce structure. Despite having the same target coordinate, the ray lengths for both reflection types differ. For the sake of convenience, only one path for a Tx- and Rx-antenna pair is plotted.

all antennas with

$$\psi(x, y, z) = \sum_{\forall tx} \sum_{\forall rx} s_{\mathrm{r}}(tx, rx) \cdot s_{\mathrm{hyp}}^*(tx, rx, p). \quad (7)$$

If the received signals from a double-bounce structure derive different target coordinates, the complex values from (7) for different antenna combinations are not in phase. This causes all the calculated correlations to be summed up imperfectly, so resulting in a lower processing gain (PG). PG describes the magnitude of the coherent summation compared to a single measurement M_0 [20], with

$$PG = \left| \frac{\psi(x, y, z)}{M_0} \right|, \quad (8)$$

and defines the image amplitude in the reconstructed image. Additionally, due to the different object geometries, a different amount of possible ray paths between Tx- and Rx-antenna exist for single and double-bounce structures. This affects the achievable PG, too.

Section II-B and II-C in II showed, that in close-range scenarios specular reflections are dominant in the reconstructed radar images compared to the other two scattering mechanisms and hence, polarimetric decomposition rather tends to detect single bounce. Volume scattering is diffuse scattering with a lower field intensity at the array, compared to the specular single bounce reflection (see Fig. 3). Specular double

bounces have a path deviation for every Tx/Rx combination compared to the focused reflection of a single bounce (see Fig. 4) and this results in a lower image amplitude by processing with (7). These mentioned issues will be compensated in the following weighting factors since in remote sensing single bounces and volume scattering are from diffuse scattering and show a similar field intensity. Furthermore, with the great distance between sensor and double bounce structure, the path deviation from a double bounce, compared to other scattering mechanisms, can be neglected.

The two described observations in close-range may result in a different image amplitude for dihedral structures and single-bounce structures, which can cause two problems. First, if both kinds of reflection take place in the same resolution cell, polarimetric decomposition tends to detect the scattering process with the higher PG. Second, the calculated double-bounce power for dihedral structures is different than from single-bounce structures with an equal radar cross section (RCS). This distorts the final polarimetric decomposition result with a wrong weighting of scattering processes.

III. ADJUSTMENT OF POLARIMETRIC REMOTE-SENSING DECOMPOSITION TO CLOSE-RANGE DECOMPOSITION

The differences explained in Section II revealed that a straightforward application of remote-sensing target decomposition would be incorrect. Due to the higher reflectivity of plane surfaces compared with dipole clouds and the path length deviations from double-bounce structures, respectively, the decomposition tends to detect the wrong scattering mechanisms. A correction of these effects can be done by introducing weighting factors into the decomposition approach from (4), which leads to a close-range adapted decomposition [15] with

$$\langle [T'_{\mathrm{aSato}}] \rangle = g_{\mathrm{s}} f_{\mathrm{s}} \langle [T] \rangle_{\mathrm{surface}} + g_{\mathrm{d}} f_{\mathrm{d}} \langle [T] \rangle_{\mathrm{double}}$$
$$+ g_{\mathrm{v}} f_{\mathrm{v}} \langle [T] \rangle_{\mathrm{vol}} + g_{\mathrm{c}} f_{\mathrm{v}} \langle [T] \rangle_{\mathrm{helix}}. \quad (9)$$

With the weighting factors g_{s}, g_{d}, and g_{v} for each scattering process, the determined powers in (5) are changed and balanced. Additionally, with an implementation of these factors into the decomposition model, the criteria for deciding which scattering process is dominating are also affected. This leads to a changed number for each detected scattering process, in addition to a changed power distribution [15].

A. DETERMINATION OF THE WEIGHTING FACTORS

Based on the observations in Section II, the weightings factors have to be calculated. To do so, quantitative values for the present errors in the close-range scenario need to be specified. Considering that decomposition uses the reconstructed radar images for every co- and cross-polarized combination, the deviations in these images can be identified.

The image amplitude obtained for every pixel in a reconstructed radar image depends on the RCS of a target and the processing gain and has been investigated in detail in [20]. The following calculations are based on this

knowledge and compare the achievable image amplitudes for single-bounces, double-bounces, and volume scattering in a close-range MIMO scenario. For this, it is simulatively investigated, how all three possible target geometries (plane surface, dihedral structure, and dipole cloud) affect the achievable processing gain. Therefore, similar to the simulations from Section II, different targets are placed at the location, and in Section IV, the experimental verification will be done. The simulated array geometry with Tx- and Rx-antenna also corresponds to the real MIMO array. Since illumination properties change for different target positions or array geometries, the following calculated weighting factors are only valid for this measurement setup, and changed array geometries also need different weighting factors. For a more complex application with moving targets or people, the described procedure must be done once in advance for different coordinates. However, since we aim to detect heavily equipped terrorists with hidden guns or explosive vests, the region of interest can be restricted to the torso. The torso position and target distance, respectively, can be determined by the reconstructed radar images. Based on this knowledge, the corresponding weighting factors can be selected for a distance-adjusted decomposition.

For a comparison between the processing gain of single and double-bounce structures, all possible ray paths between Tx- and Rx-antennas need to be known. Therefore, each target is placed at the position, where for the real measurement different threat objects will be located later. Fig. 5 shows the possible signal paths for both target structures. As it can be seen, the dihedral structure and the plate produce reflections that are not focused in one point. This effect has also been described for the metal plate in [20] and it causes a phase mismatch between the measured signal and the focusing term, as shown in (7) for an ideal point scatterer, and results in a reduced PG. The PGs achieved for single and double-bounce structures in the simulation are compared against each other. Additionally, for improved results, the dihedral structure was rotated for 90° around the line of sight to the MIMO array and the mean result for both rotation angles (0 and 90°) was used. The ratio between single and double-bounce PG yields

$$PG_{D,S} = \frac{PG_D}{PG_S} = 0.8 = g_d. \tag{10}$$

Hence, as explained in Section II II-C, reflections obtained from single-bounce structures result in a higher image amplitude compared with those obtained from dihedral structures. Therefore, the weighting factor g_d needs to increase the power P_d for detected double-bounces and is determined by $PG_{D,S}$. This amplifies the searched double-bounce coefficient f_d by

$$f_d \propto \frac{1}{g_d \langle [T] \rangle_{\text{double}}}, \tag{11}$$

where $\langle [T] \rangle_{\text{double}}$ is the measured coherency matrix with the entries for the double-bounces.

The same evaluation is done for volume scattering. For an ideal comparison between all scattering processes, the previous single-bounce target is compared with a diffuse scattering
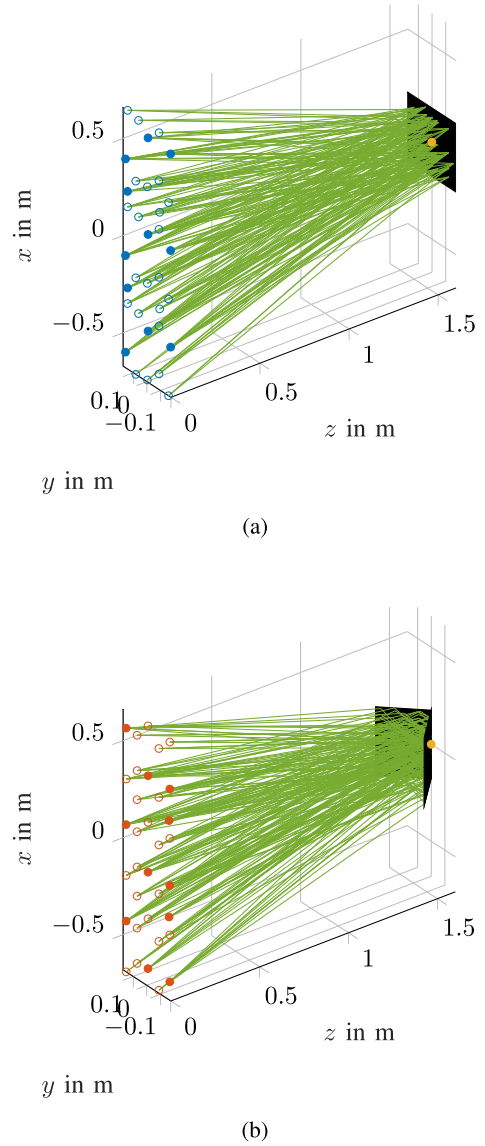

(a)

(b)

FIGURE 5. All possible signal paths for every (a) horizontal and (b) vertical polarized Tx- and Rx-antenna combination, and the different scattering targets. The dominating specular reflection in the close-range produces many possible ray paths with different ray lengths.

dipole cloud. Since the scattering properties for the dipole cloud change with the surface roughness h (see Fig. 6), the following consideration has to be taken into account: with respect to the roughness h, an incident wave is reflected at two possible height positions [21]. The total length difference for the two scattered waves is $2\Delta r$ and the phase difference is therefore

$$\Delta\varphi = \frac{2\pi}{\lambda} \cdot 2\Delta r = \frac{4\pi \cdot h}{\lambda \cdot \sin\gamma}, \tag{12}$$

with the wavelength λ and the incident angle γ [21]. For a flat surface with $h_{\text{flat}} = 0$, the phase difference $\Delta\varphi_{\text{flat}} = 0$. Whereas for a roughness of $\lambda/4$ and normal incidence, the phase difference $\Delta\varphi_{\lambda/4} = \pi$ and destructive interference is present. In terms of reflected power, these are the both limiting
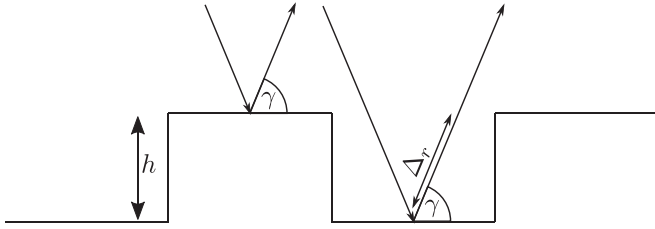
FIGURE 6. Simplified illustration for possible ray paths with different lengths for a rough surface [21].

cases for a maximal and minimal reflected field intensity, and they have to be considered for the calculation of the weighting factor g_v.

The simulation explained in Section II II-B and shown in Fig. 2 and Fig. 3 is used for a comparison of the difference for the intensities in the reconstructed radar images by specular and diffuse reflection. An electric field is emitted sequentially by every Tx-antenna of the MIMO array and is scattered by a perfect electric conducting plane surface, and a rough dipole cloud, respectively. The reflectivity of the dipoles is normally distributed between 0 and 1, and the surface roughness is 0 and $\lambda/4$, respectively. The simulated electric field intensity and phase of every Rx-antenna are then used to calculate and compare the achievable processing gain PG_S for the flat surface and PG_V for the dipole cloud scatterer. The simulation yields a value of

$$PG_{V,S} = \frac{PG_V}{PG_S} = \begin{cases} 0.5 & \text{if h} = 0. \\ 0.017 & \text{if } h = \lambda/4. \end{cases} \quad (13)$$

As can be seen in (13), there is no unique solution without an a priori knowledge about the dipole surface roughness in the later investigated security scenario. Since f_v is non-linear increased with a $1/g_v$ dependency, the mean value for this is used as a trade-off for the results in (13). The weighting factor g_v can then be calculated by

$$\frac{1}{g_v} = \frac{1}{0.5 - 0.017} \int_{0.017}^{0.5} \frac{1}{g_v} dg_v = 7, \quad (14)$$

and $g_v = 0.14$, respectively.

As it was shown that single-bounce is the dominating scattering process compared to the dihedral structure and dipole cloud, the determined value for f_s should not be increased even further. This leads the related weighting factor to be

$$g_s = 1. \quad (15)$$

B. DECOMPOSITION ALGORITHM
The adapted decomposition technique is based on the decomposition method by Sato et al. [9]. Hence, the decomposition algorithm is very similar to the original algorithm, but with the introduced weighting factors in (9) the calculation process changes. A detailed explanation of the original approach can be found in [9]. Here, a short summary of the novel approach from [15] will be given, and a flowchart for the here described close-range decomposition algorithm can be seen in Fig. 10.

Equation 9 for the close-range adapted decomposition method leads to the following equations for the coherency matrix elements:

$$T_{\text{aSato},11} = g_s f_s + g_d f_d |\alpha|^2 + g_v f_v a$$

$$T_{\text{aSato},12} = g_s f_s \beta^* + g_d f_d \alpha + g_v f_v b$$

$$T_{\text{aSato},22} = g_s f_s |\beta|^2 + g_d f_d + g_v f_v c + g_v \frac{1}{2} f_c$$

$$T_{\text{aSato},23} = \pm g_v j \frac{1}{2} f_c$$

$$T_{\text{aSato},33} = g_v f_v d + g_v \frac{1}{2} f_c. \quad (16)$$

The parameters β and α describe the ratios for the horizontal and vertical reflection coefficients for single and double-bounces [5]. The assumed volume scattering model in the decomposition is determined by the parameters a, b, c, and d and chosen as described in [9].

First, the T_{33} rotation, as described in [12], is applied to the calculated coherency matrix $\langle[T]\rangle$ and yields the rotated coherency matrix $\langle[T']\rangle$. After calculating the helix scattered power P_c with

$$P_c = f_c = \frac{2}{g_v}|\Im(T'_{23})|, \quad (17)$$

the dominating scattering process (surface or double-bounce) has to be determined. However, since the weighting factors are introduced, the value of C'_{13} [9] used so far is changed to

$$C'_{13} = g_s f_s \beta + g_d f_d \alpha, \quad (18)$$

and can no longer be evaluated just by the sign of its real part. With $g_s \neq g_d$ and the general reflection case of $\beta = 1, \alpha = -1$ [5], no sign conversion occurs at the limit case $f_d = f_s$, as C'_{13} is turned into

$$C'_{13} = g_s f_s - g_d f_d. \quad (19)$$

Hence, the value of $C_{33} = g_s f_s + g_d f_d$ is also taken into account. For the investigated case of $f_s = f_d$, C'_{13} and C'_{33} can be rewritten as

$$C'_{13}(f_d = f_s) = f_s(g_s - g_d)$$

$$C'_{33}(f_d = f_s) = f_s(g_s + g_d). \quad (20)$$

By combining these equations, C_0 can be obtained by

$$C_0 = \frac{C'_{13}}{g_s - g_d} - \frac{C'_{33}}{g_s + g_d} = \frac{2g_s g_d}{g_s^2 - g_d^2}(f_s - f_d). \quad (21)$$

It can be seen, that the sign of $\Re(C_0)$ changes at $f_s = f_d$. For a determination of the dominating scattering process, the weighting factors g_s and g_d have to be considered. With reference to (21), dihedral scattering is dominating if

$$\Re(C_0) < 0 \land g_d/g_s < 1 \text{ or}$$

$$\Re(C_0) > 0 \land g_d/g_s > 1, \quad (22)$$

TABLE 1. Criterion for the Determination of the Dominating Scattering Process [15]

$\Re(T_0)$	g_d/g_s	dominating process	set parameter
< 0	< 1	double-bounce	$\beta = 0$
< 0	> 1	single-bounce	$\alpha = 0$
< 0	< 1	single-bounce	$\alpha = 0$
< 0	> 1	double-bounce	$\beta = 0$

and leads to the dihedral volume scattering model with $c = 7/15$ and $d = 8/15$:

$$\langle[T]\rangle_{\text{vol}} = \begin{bmatrix} a & b & 0 \\ b & c & 0 \\ 0 & 0 & d \end{bmatrix} = \frac{g_d}{g_v}\frac{1}{15}\begin{bmatrix} 0 & 0 & 0 \\ 0 & 7 & 0 \\ 0 & 0 & 8 \end{bmatrix}. \quad (23)$$

If dihedral scattering is not dominating, $\langle[T]\rangle_{\text{vol}}$ is modeled with respect to the ratio of $\langle|S_{VV}|^2\rangle/\langle|S_{HH}|^2\rangle$ as a dipole cloud as described in [9]. With the scattering model $\langle[T]\rangle_{\text{vol}}$ now defined, f_v can be straightforwardly calculated by T'_{33} with

$$f_v = \frac{T'_{33} - g_v\frac{1}{2}f_c}{g_v d}. \quad (24)$$

Next, due to four unknowns f_s, f_d, α, and β in the remaining three equations from (16), one parameter has to be set. Hence, again (21) is used for determination if single or double-bounce is dominating. Removing the calculated volumetric part by subtracting it from $\langle[T']\rangle$, $\langle[T'']\rangle$ contains only single or double-bounce information. Thus, the C_0 criterion can be rewritten as

$$T_0 = \frac{T''_{11} - T''_{22}}{2(g_s - g_d)} - \frac{T''_{11} - 2\Re(T''_{12}) + T''_{22}}{2(g_s + g_d)}, \quad (25)$$

and evaluated by Tab. I for the dominating scattering process. Setting α or β to zero, f_s and f_d can be calculated. The total power distribution P_t of each scattering process can be determined by

$$P_t \propto T'_{11} + T'_{22} + T'_{33} = P_s + P_d + P_v + P_c$$

$$= g_s f_s(1 + |\beta|^2) + g_d f_d(1 + |\alpha|^2)$$

$$+ g_v(a + c + d)f_v + g_v f_c. \quad (26)$$

IV. EXPERIMENTAL VERIFICATION

The derived decomposition technique is now verified. First, an evaluation for different test structures is analyzed and afterwards, scenarios with a dummy and a real human wearing different objects on their body are investigated.

A. MIMO IMAGING SYSTEM

For the measurements, a full polarimetric MIMO array for the frequency range from $4-12$ GHz was used. The array was built from four frontend tiles with 4 Tx- and 8 Rx-antennas per polarization, resulting in a total of 32 Tx- and 64 Rx-antennas. Their full width at half maximums (FWHM) are 49° and 48° in the E- and H-plane, respectively. An image of the antennas, the array geometry, and position can be seen in Fig. 7.
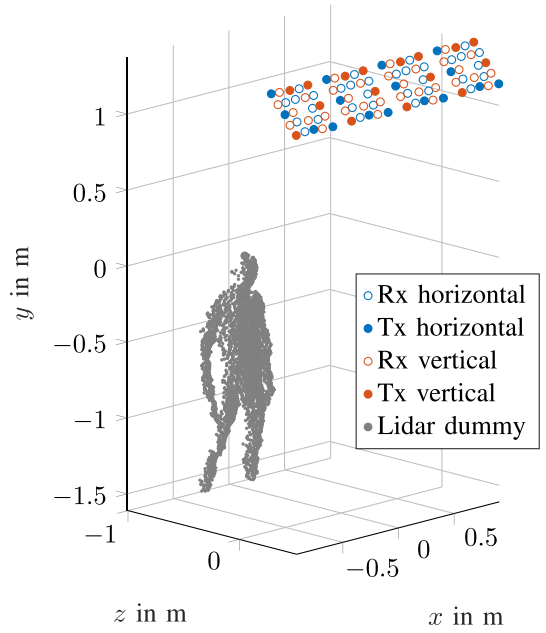
(a)

(b)

FIGURE 7. Array geometry and position relative to a later investigated dummy are shown in (a). Image of the tile with horizontal and vertical polarized Tx- and Rx-antennas (b).

Additional information of the key parameters for the imaging system can be found in Tab. II.

Imaging for every polarimetric combination (HH, VV, VH, HV) was done by Hilbert transforming the sampled real pulse, backprojecting, and a weighting with the phase coherence factor [22] for an improved side-lobe suppression. The coherency matrix is calculated from the reconstructed images by (3) and used for the polarimetric target decomposition.

B. POLARIMETRY RESULTS FOR TEST STRUCTURES

For an investigation of the improvement achieved in target decomposition, different obstacles were placed onto a metal plate (see Fig. 8). In particular, the sphere, dihedral structures, and bag of screws are of interest, because they represent the targets for single-bounce, double-bounce, and volume

TABLE 2. Key Parameters of the Used MIMO Imaging System

Signal waveform	Pulse
Frequency range	4 GHz to 12 GHz
Tx antennas per polarization	16
Rx antennas per polarization	32
Antennas FWHM (E-plane)	49°
Antennas FWHM (H-plane)	48°
MIMO array total width	1.8 m
MIMO array total height	32.5 cm
Inclination angle of MIMO array	45°
Range resolution	1.8 cm
Lateral resolution (x)	1.7 cm
Lateral resolution (y)	7.4 cm
Frame rate	13 frames/second
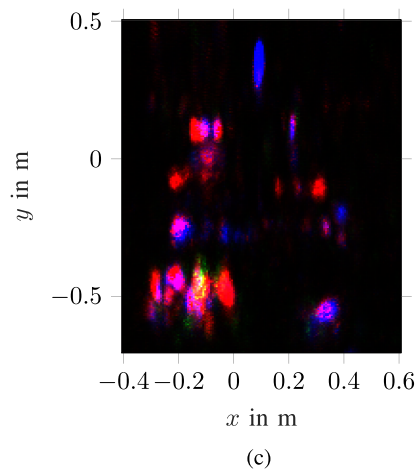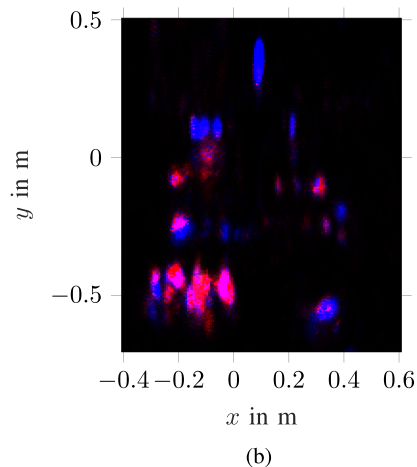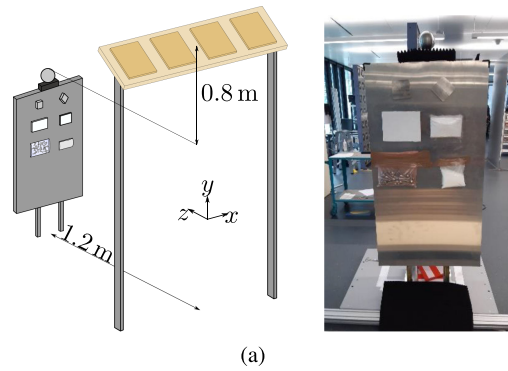
scattering. The other objects are different polymers and imitate explosives. With the oblique observation angle of the MIMO array, the metal plate reflects the incident wave towards the ground and not back to the antennas. Hence, its strong reflection won't be seen in the reconstructed image. Whereas objects placed on the metal plate reflect back to the array due to their surface orientation or dihedral structure on the metal plate.

A comparison of the decomposition results can be seen in Fig. 8. The colors are assigned as follows: blue for single-bounce, red for double-bounce, and green for volume scattering. With the new proposed decomposition algorithm, a significant improvement in the target classification can be achieved. The sphere at $x = 0.1$ m, $y = 0.4$ m correctly remains a single-bounce for both algorithms. The dihedral structure at $x = -0.1$ m, $y = 0.1$ m is changed correctly to a double-bounce with the new decomposition algorithm. Furthermore, the screw bag at $x = -0.2$ m, $y = -0.5$ m has an increased volume scattering rate. Whereas with the conventional decomposition algorithm no volume scattering was detected.

Merely, the 45° tilted dihedral structure at $x = 0.2$ m, $y = 0.1$ m has a single and double-bounce signature. This geometry was not further investigated in Section III and due to the different orientation of this object, there is a need to increase the detection of this double-bounce structure. Setting g_d to a lower value than calculated in (10), a pure double-bounce can be detected. Nevertheless, many voxels were assigned with a new dominating scattering process and the total double and volume scattering power was increased, yielding in an improved polarimetric decomposition result.

C. POLARIMETRY RESULTS FOR SECURITY SCENARIOS

Having shown that the adapted decomposition technique improves the results obtained for defined polarimetric target structures, security scenarios are now investigated. A dummy and a human carry different objects around their torso, such as a knife, a gun, or a block of modeling clay covered with screws, imitating explosives with shrapnel (see. Fig. 9(a) to (e)). The size of screws and bolts were chosen so that they act as dipoles or as a dipole cloud and have a diameter between

(a)

(b)

(c)

FIGURE 8. Test setup and image from test structures placed onto a metal plate (a). Polarimetric results with decomposition method described in [9] (b) and the new close-range adapted decomposition technique (c).

4 mm to 8 mm and a length between 3 cm to 5 cm. Additionally, the objects were hidden under a layer of clothes and a vest. The dielectric properties of human skin are $\varepsilon_r = 25$ at 10 GHz [23]. The reflectance between skin and air for normal incidence, which is the dominating specular reflection in close-range imaging, can be calculated by Fresnel equations to $\Gamma = |\frac{\sqrt{25}-1}{\sqrt{25}+1}|^2 = 0.44$. For comparison, the copolarized reconstructed images are also shown in Fig. 9(f) to (k). They
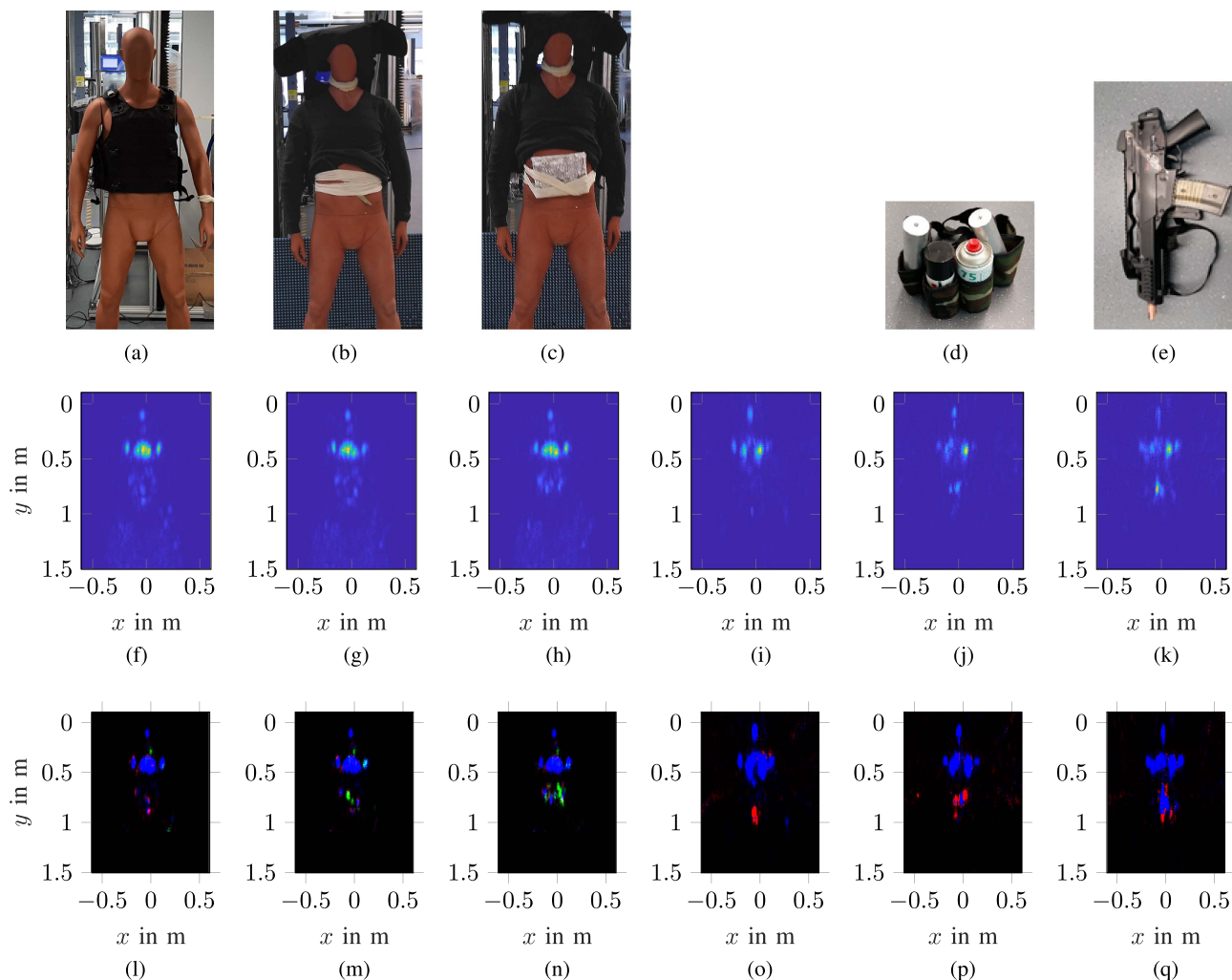
FIGURE 9. Photos (a) - (e), copolarized radar images (f) - (k) and polarimetric results (l) - (q) for a dummy and a human wearing different objects under clothes. The following scenarios were investigated: a dummy without any threat objects (a), a dummy with a knife (b), and a dummy with a block of modeling clay covered with screws (c), and a human without any threat objects (not shown), a human with a vest with metallic cans forming a suicide vest(d), and a human with a gun (e).

represent imaging results, that can be achieved with state-of-the-art security scanners.

The results for the dummy and human without any hidden objects serve as a reference point for when there are no potential security dangers. Since they represent persons without any hidden objects. Due to the array position and orientation, only few reflections can be seen in the radar images, and an evaluation for potential security threats would appear to be difficult. In most cases, only the specular reflections from the body surface perpendicular to the array, namely the forehead, breast, and shoulder, are recognizable. The reflections from the worn objects have small dimensions and are weak, and the diffuse scattering from the clothes makes recognition of the reflections difficult. With the polarimetric decomposition, worn objects can clearly be detected. The knife and screws increase the determined volume scattering power. The gun and the cans of the suicide belt generate a dihedral structure with the human body and produce a double-bounce. The

dimensions of the gun are so large, that from the plane surface a single-bounce is also detected, and correctly only a double-bounce is detected at the outer edge. Taking the polarimetric scattering information into account, hidden weapons or explosives can be more easily detected.

In our measurement scenario, test structures and dummy were static and the human test person also tried to stand still. However, since this system tries to investigate walking persons, further considerations on possible artifacts through motion have to be done. Due to the measurement time of approximately 77 ms for a full scan of all Tx-antennas, a person with a walking speed of 2 m/s moves 15 cm during the measurement. This shift causes motion blur in the reconstructed radar images and deteriorates the image quality. However, in [24] it was shown that this issue can be compensated by separating the measured data into smaller data segments and shifting the antenna positions with respect to the detected target velocity. With this technique, an effective
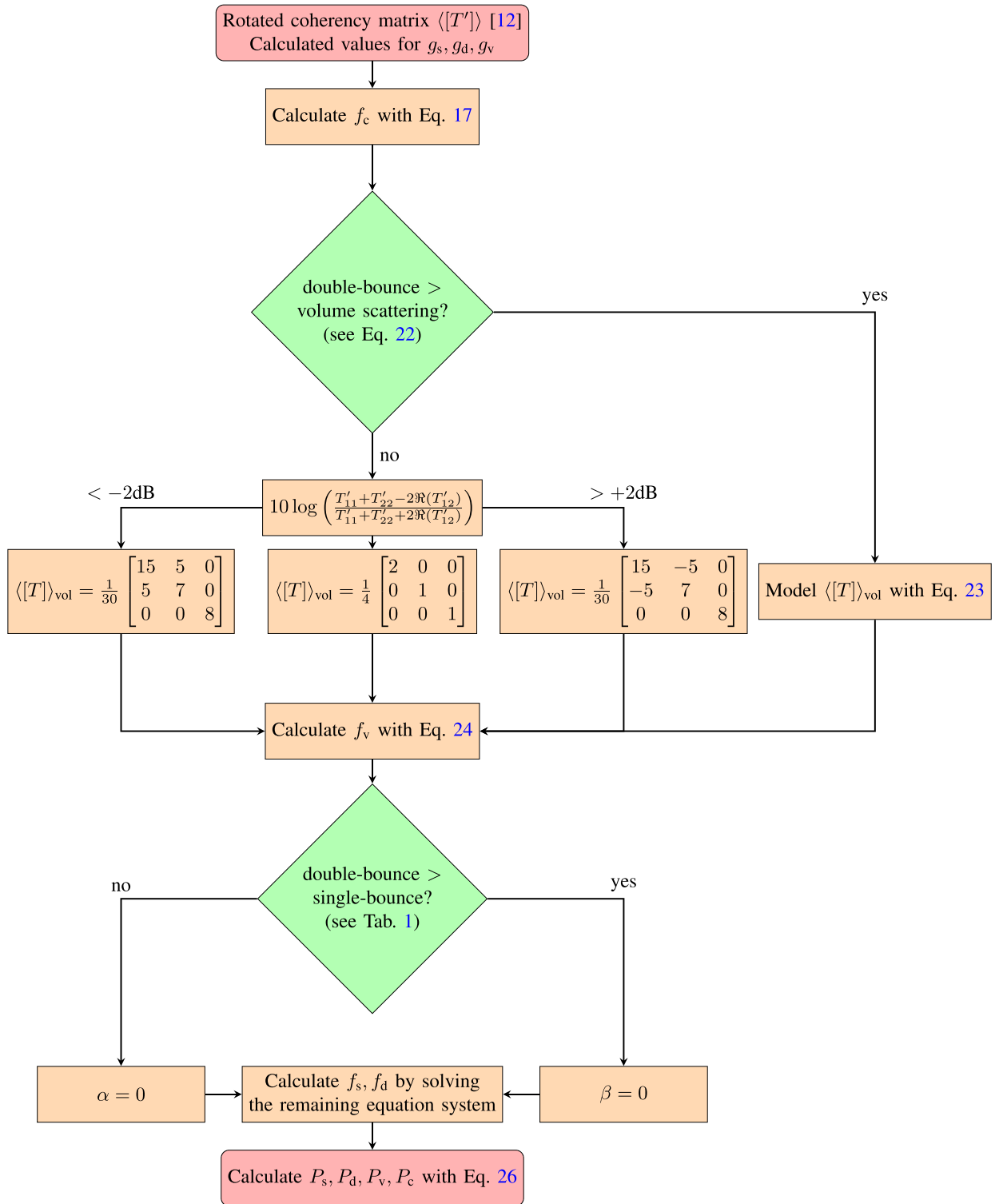
Rotated coherency matrix $\langle[T']\rangle$ [12]
Calculated values for $g_{\mathrm{s}}, g_{\mathrm{d}}, g_{\mathrm{v}}$

Calculate f_{c} with Eq. 17

double-bounce >
volume scattering?
(see Eq. 22)

yes

no

$$10 \log\left(\frac{T'_{11}+T'_{22}-2\Re(T'_{12})}{T'_{11}+T'_{22}+2\Re(T'_{12})}\right)$$

$< -2\mathrm{dB}$

$> +2\mathrm{dB}$

$$\langle[T]\rangle_{\mathrm{vol}} = \frac{1}{30}\begin{bmatrix} 15 & 5 & 0 \\ 5 & 7 & 0 \\ 0 & 0 & 8 \end{bmatrix}$$

$$\langle[T]\rangle_{\mathrm{vol}} = \frac{1}{4}\begin{bmatrix} 2 & 0 & 0 \\ 0 & 1 & 0 \\ 0 & 0 & 1 \end{bmatrix}$$

$$\langle[T]\rangle_{\mathrm{vol}} = \frac{1}{30}\begin{bmatrix} 15 & -5 & 0 \\ -5 & 7 & 0 \\ 0 & 0 & 8 \end{bmatrix}$$

Model $\langle[T]\rangle_{\mathrm{vol}}$ with Eq. 23

Calculate f_{v} with Eq. 24

double-bounce >
single-bounce?
(see Tab. 1)

no

yes

$\alpha = 0$

Calculate $f_{\mathrm{s}}, f_{\mathrm{d}}$ by solving
the remaining equation system

$\beta = 0$

Calculate $P_{\mathrm{s}}, P_{\mathrm{d}}, P_{\mathrm{v}}, P_{\mathrm{c}}$ with Eq. 26

FIGURE 10. Flow chart for the close-range adapted polarimetric target decomposition.

and fast motion blur suppression was applied to simulated and real measured data. The achievable image quality for moving persons can then be expected as good as for standing persons shown here and hence, promising results as shown in Fig. 9 are achievable.

V. CONCLUSION

This paper presented a novel approach for security controls with an overhead observation and a polarimetric target decomposition. It was shown that if humans are equipped with guns or explosives with shrapnel, three possible scattering

mechanisms (single-bounce, double-bounce, and volume scattering) are present. Whereas a person without any hidden object almost has only a single-bounce signature, since the skin acts as a plane surface without any edges. Double-bounce can be detected from weapons with big dimensions such as suicide vests or guns. Their surface and the human body create a dihedral structure and can clearly be identified in the decomposition. Smaller metallic objects like knives or shrapnel increase the detected volumetric power in the image due to their dipole-like geometry. Hence, polarimetric decomposition is well suited for application in security scenarios.

However, the usage of polarimetric target decomposition had to be adapted to this novel use case. The differences in close-range and remote-sensing lead to an incorrect decomposition result if no correction is applied. Since reconstructed radar images for every polarization combination are the initial point for the decomposition, differences in the obtained images and scattering processes were investigated. It was shown that strong specular reflections dominate in close-range imaging, while double-bounce and volume scattering produce lower image amplitudes. For that reason, an existing decomposition algorithm was changed, so that all scattering mechanisms are equally represented and weighted in the decomposition. This was done by introducing weighting factors to the decomposition model. Their values were determined simulatively and they describe the ratios for the achievable processing gains for each scattering mechanism. By adding these factors to the model, improved decomposition results were achieved for defined test structures and security scenarios.

The application of the shown security scanner in crowded places demands for an automatic detection of threat objects with a low false alarm rate. The obtained results in Fig. 9 showed, that polarimetric decomposition reliably detects hidden, carried objects and facilitates for humans a possible threat recognition. A comparison of the benefit of the additional information from polarimetric results compared to copolarized radar images and how to use them in an automatic detection scenario, have to be investigated in the future. However, since with a full polarimetric array more information is collected about a target, an additional improvement for a more robust detection algorithm can be expected.

The application of this technology in crowded places demands very reliable threat detection. Not investigated scenarios, e.g. everyday objects like keys and backpacks could be confused with explosives or guns. Even if it was not needed for the investigated scenarios here, the neglected helix scattering power may contain additional, useful information, that helps to differentiate between these objects. Additionally, further improvements may be made by investigating other decomposition techniques with different scattering models.

ACKNOWLEDGMENT

REFERENCES

[1] S. S. Ahmed, "Personnel screening with advanced multistatic imaging technology," *Proc. SPIE* vol. 8715, 2013, pp. 84–89, doi: 10.1117/12.2018054.

[2] F. Gumbmann and S. S. Ahmed, "Walk through screening with multistatic mmW technology," *Proc. SPIE*, vol. 9993, 2016, pp. 39–44, doi: 10.1117/12.2247183.

[3] S. R. Cloude and E. Pottier, "A review of target decomposition theorems in radar polarimetry," *IEEE Trans. Geosci. Remote Sens.*, vol. 34, no. 2, pp. 498–518, Mar. 1996, doi: 10.1109/36.485127.

[4] S.-W. Chen, Y.-Z. Li, X.-S. Wang, S.-P. Xiao, and M. Sato, "Modeling and interpretation of scattering mechanisms in polarimetric synthetic aperture radar: Advances and perspectives," *IEEE Signal Process. Mag.*, vol. 31, no. 4, pp. 79–89, Jul. 2014, doi: 10.1109/MSP.2014.2312099.

[5] A. Freeman and S. L. Durden, "Three-component scattering model to describe polarimetric SAR data," *Proc. SPIE*, vol. 1748, 1993, pp. 213–224, doi: 10.1117/12.140618.

[6] Y. Yamaguchi, T. Moriyama, M. Ishido, and H. Yamada, "Four-component scattering model for polarimetric SAR image decomposition," *IEEE Trans. Geosci. Remote Sens.*, vol. 43, no. 8, pp. 1699–1706, Aug. 2005, doi: 10.1109/TGRS.2005.852084.

[7] S.-W. Chen, X.-S. Wang, S.-P. Xiao, and M. Sato, "General polarimetric model-based decomposition for coherency matrix," *IEEE Trans. Geosci. Remote Sens.*, vol. 52, no. 3, pp. 1843–1855, Mar. 2014, doi: 10.1109/TGRS.2013.2255615.

[8] G. Singh and Y. Yamaguchi, "Model-based six-component scattering matrix power decomposition," *IEEE Trans. Geosci. Remote Sens.*, vol. 56, no. 10, pp. 5687–5704, Oct. 2018, doi: 10.1109/TGRS.2018.2824322.

[9] A. Sato, Y. Yamaguchi, G. Singh, and S.-E. Park, "Four-component scattering power decomposition with extended volume scattering model," *IEEE Geosci. Remote Sens. Lett.*, vol. 9, no. 2, pp. 166–170, Mar. 2012, doi: 10.1109/LGRS.2011.2162935.

[10] J. Chen, H. Zhang, and C. Wang, "An improved four-component decomposition with distributed double-bounce scattering model," in *Proc. Int. Conf. Comput. Vis. Remote Sens.*, 2012, pp. 344–349, doi: 10.1109/CVRS.2012.6421287.

[11] W. Han, H. Fu, J. Zhu, C. Wang, and Q. Xie, "Polarimetric SAR decomposition by incorporating a rotated dihedral scattering model," *IEEE Geosci. Remote Sens. Lett.*, vol. 19, pp. 1–5, 2022, Art no. 4005505, doi: 10.1109/LGRS.2020.3035567.

[12] Y. Yamaguchi, A. Sato, W.-M. Boerner, R. Sato, and H. Yamada, "Four-component scattering power decomposition with rotation of coherency matrix," *IEEE Trans. Geosci. Remote Sens.*, vol. 49, no. 6, pp. 2251–2258, Jun. 2011, doi: 10.1109/TGRS.2010.2099124.

[13] C. A. Balanis, *Antenna Theory Analysis and Design*. Hoboken, NJ, USA: Willey, 1997.

[14] F. Xu and Y.-Q. Jin, "Deorientation theory of polarimetric scattering targets and application to terrain surface classification," *IEEE Trans. Geosci. Remote Sens.*, vol. 43, no. 10, pp. 2351–2364, Oct. 2005, doi: 10.1109/TGRS.2005.855064.

[15] J. Adametz, "Polarimetric decomposition techniques for close-range radar imaging systems," Ph.D. dissertation Friedrich-Alexander-Universität Erlangen-Nürnberg, Erlangen, Germany, 2018.

[16] M. Umemura, Y. Yamaguchi, and H. Yamada, "Model-based target classification using polarimetric similarity with coherency matrix elements," *IEICE Commun. Exp.*, vol. 8, no. 3, pp. 73–80, Jan. 2019, doi: 10.1587/comex.2018XBL0152.

[17] W. C. Chew, *Waves and Fields in Inhomogeneous Media*. Piscataway, NJ, USA: IEEE Press, 1995.

[18] J. S. Lee and E. Pottier, *Polarimetric Radar Imaging, From Basics to Applications*. Boca Raton, FL, USA: CRC Press, 2009.

[19] D. M. Sheen, D. L. McMakin, and T. E. Hall, "Three-dimensional millimeter-wave imaging for concealed weapon detection," *IEEE Trans. Microw. Theory Techn.*, vol. 49, no. 9, pp. 1581–1592, Sep. 2001, doi: 10.1109/22.942570.

[20] S. S. Ahmed, A. Schiessl, and L.-P. Schmidt, "Illumination properties of multistatic planar arrays in near-field imaging applications," in *Proc. 7th Eur. Radar Conf.*, 2010, pp. 29–32.

[21] H. Klausing and W. Holpp, *Radar Mit Realer Und Synthetischer Apertur*. Berlin, Germany: Oldenbourg Wissenschaftsverlag, 2010, pp. 39–40.

[22] J. Camacho, M. Parrilla, and C. Fritsch, "Grating-lobes reduction by application of phase coherence factors," in *Proc. IEEE Int. Ultrasonics Symp.*, 2009, pp. 341–344, doi: 10.1109/ULTSYM.2009.5441770.

[23] S. A. R. Naqvi, M. Manoufali, B. Mohammed, A. T. Mobashsher, D. Foong, and A. M. Abbosh, "In vivo human skin dielectric properties characterization and statistical analysis at frequencies from 1 to 30 GHz," *IEEE Trans. Instrum. Meas.*, vol. 70, pp. 1–10, 2021, Art. no. 6001710, doi: 10.1109/TIM.2020.3036767.

[24] T. Sumiya, K. Ogura, S. Yamanouchi, N. Khan, M. Ariyoshi, and T. Nomura, "Motion blur suppression accommodating to fast radar imaging for walk-through concealed weapon detection," in *Proc. IEEE Radar Conf.*, 2020, pp. 1–6, doi: 10.1109/RadarConf2043947.2020.9266439.

KONSTANTIN ROOT received the B.Eng. degree in electrical engineering from the Ostbayerische Technische Hochschule Regensburg, Regensburg, Germany, in 2017, and the M.Sc. degree in electrical engineering from Friedrich-Alexander Universität (FAU) Erlangen-Nürnberg, Erlangen, Germany, in 2019. He was a Research Scientist with the Institute of Microwaves and Photonics, FAU. His research interests include radar signal processing and polarimetric radar imaging.

JULIAN ADAMETZ received the Dipl.-Ing. (M.Sc.) degree in electrical engineering from the Friedrich-Alexander-Universität (FAU) Erlangen-Nürnberg, Erlangen, Germany, in 2009, and the Ph.D. degree in 2018, for his thesis "Polarimetric Decomposition Techniques for Close-Range Radar Imaging Systems." He joined the Institute of Microwaves and Photonics, FAU, in the same year. He joined the Brose Fahrzeugteile SE and Co. KG as a Project Manager with the Advanced Development Sensor Technologies Department in 2019. His research interests include millimeter-wave imaging, polarimetric imaging, nondestructive testing, and automotive radar applications.

FRANK GUMBMANN received the Diploma and the Ph.D. degree in electrical engineering from the Friedrich-Alexander-Universität (FAU) Erlangen-Nürnberg, Erlangen, Germany, in 2005 and 2011, respectively. From 2005 to 2012, he was with the Institute of Microwaves and Photonics, FAU, dealing with the design of sparse antenna arrays for short-range imaging and radar signal processing. Since 2012, he has been an R&D Engineer with the Microwave Imaging Department, Rohde and Schwarz, Munich, Germany. His research interests include millimeter-wave measurement techniques, radar imaging systems, and radar signal processing.

INGRID ULLMANN received the M.Sc. and Ph.D. degrees from Friedrich-Alexander-Universität (FAU) Erlangen-Nürnberg, Erlangen, Germany, in 2016 and 2021, respectively. She is currently a Postdoc with the Institute of Microwaves and Photonics at FAU. Her research interests include radar imaging and radar signal processing for nondestructive testing, security, medical and automotive applications. She is group leader of the Research Group Radar and Imaging Systems at the Institute of Microwaves and Photonics and is a reviewer for the European Radar Conference (EuRAD) and various journals in the field of microwaves. Dr. Ullmann was the recipient of the Argus Science Award (sponsored by Airbus Defense and Space, now Hensoldt) for her master thesis in 2016 and the Best Paper Award of the European Radar Conference in 2019.

MARTIN VOSSIEK (Fellow, IEEE) received the Ph.D. degree from Ruhr-Universität Bochum, Bochum, Germany, in 1996. In 1996, he joined Siemens Corporate Technology, Munich, Germany, where he was the Head of the Microwave Systems Group from 2000 to 2003. Since 2003, he has been a Full Professor with Clausthal University, Clausthal-Zellerfeld, Germany. Since 2011, he has also been the Chair of the Institute of Microwaves and Photonics (LHFT), Friedrich-Alexander-Universität Erlangen-Nürnberg (FAU), Erlangen, Germany. He has authored or coauthored more than 300 articles. His research has led to over 90 granted patents. His research interests include radar, transponder, RF identification, communication, and wireless locating systems. Dr. Vossiek is currently a Member of the German National Academy of Science and Engineering (acatech) and the German Research Foundation (DFG) Review Board. He is also a Member of the German IEEE MICROWAVE THEORY AND TECHNIQUES (MTT)/IEEE TRANSACTIONS ON ANTENNAS AND PROPAGATION Chapter Executive Board and the IEEE MTT Technical Committees MTT-24 Microwave/mm-Wave Radar, Sensing, and Array Systems, MTT-27 Connected and Autonomous Systems (as the Founding Chair), and the MTT-29 Microwave Aerospace Systems. He also serves on the Advisory Board of the IEEE CRFID Technical Committee on Motion Capture & Localization. He is a member of organizing committees and technical program committees for many international conferences. He has served on the review boards for numerous technical journals. He was the recipient of more than ten best paper prizes and several other awards. For example, he was the recipient of the 2019 Microwave Application Award from the IEEE MTT Society for Pioneering Research in Wireless Local Positioning Systems. From 2013 to 2019, he was an Associate Editor for IEEE TRANSACTIONS ON MICROWAVE THEORY AND TECHNIQUES.